# Topological surface states and weak thermal phonon anharmonicity of low-lying phonons in GeSb$_2$Te$_4$

Peng Wu (吴鹏) [1,2,*,†] Tongrui Li (李彤瑞),[1,*] Bo Zhang (张波),[1] Jie Sun (孙杰),[3] Shengtao Cui (崔胜涛),[1] Yi Liu (刘毅),[1]
Kunling Peng (彭坤岭),[4,†] Liwei Deng (邓力玮),[5] Jiameng Wang (王佳萌),[5] Masao Yonemura (米村雅雄),[6]
Lidong Zhang (张李东),[1] Takashi Kamiyama (神山崇),[6] Shan Qiao (乔山),[5,7] and Zhe Sun (孙喆)[1,8,9,10,†]

[1]*National Synchrotron Radiation Laboratory, University of Science and Technology of China,
Hefei, Anhui 230026, People's Republic of China*
[2]*Hefei Innovation Research Institute, Beihang University, Hefei, Anhui 230013, People's Republic of China*
[3]*Institute of Engineering Innovation, Graduate School of Engineering, The University of Tokyo, Bunkyo-ku, Tokyo 113-0032, Japan*
[4]*Interdisciplinary Center for Fundamental and Frontier Sciences, Nanjing University of Science and Technology,
Jiangyin, Jiangsu 214443, People's Republic of China*
[5]*State Key Laboratory of Functional Materials for Informatics, Shanghai Institute of Microsystem and Information Technology,
Chinese Academy of Sciences, Shanghai 200050, People's Republic of China*
[6]*Materials & Life Science Division, J-PARC Center, High Energy Accelerator Research Organization (KEK),
Tokai, Ibaraki 319-1106, Japan*
[7]*School of Physical Science and Technology, ShanghaiTech University, Shanghai 201210, People's Republic of China*
[8]*CAS Key Laboratory of Strongly-Coupled Quantum Matter Physics, University of Science and Technology of China,
Hefei, Anhui 230026, People's Republic of China*
[9]*Hefei National Laboratory, University of Science and Technology of China, Hefei 230088, People's Republic of China*
[10]*Collaborative Innovation Center of Advanced Microstructures, Nanjing 210093, People's Republic of China*

Recently, solid crystalline GeSb$_2$Te$_4$ was found to host topological surface states and low lattice thermal conductivity. In this work, we conducted comprehensive investigations on the electronic structures and lattice dynamics of GeSb$_2$Te$_4$. By combining synchrotron-based and spin-resolved angle-resolved photoemission spectroscopy and first-principles calculations, we observed distinctive topological surface states with significant spin polarization near the Fermi level. Furthermore, our temperature-dependent Raman scattering measurements revealed weak changes in linewidths of low-energy optical modes, indicating the weak temperature-dependent phonon anharmonicity of those modes. This finding is further supported by our lattice thermal conductivity calculation, which explains the minor variation in lattice thermal conduction in the high-temperature region. Our study sheds light on the exotic electronic and lattice dynamics of GeSb$_2$Te$_4$, potentially leading to new insights into its technological applications.

## I. INTRODUCTION

To date, most studies on GeSb$_2$Te$_4$ have concentrated on its phase change-related properties because its electrical resistivity could drastically vary over six orders of magnitude from the insulating amorphous phase to the metallic crystalline hexagonal phase [1–4]. However, hexagonal crystalline GeSb$_2$Te$_4$ also hosts various fascinating physical properties. For instance, it is theoretically predicted to be a topological insulator [5,6], and the topological band structures have been verified by angle-resolved photoemission spectroscopy (ARPES), showing the surface Dirac cone located at 0.45 eV above the Fermi level [7]. In addition, single crystalline GeSb$_2$Te$_4$ was reported to hold a low lattice thermal conductivity with values of 1.4 to 1.53 and 0.4 to 0.73 W m$^{-1}$ K$^{-1}$

along the *a*-axis and *c*-axis, respectively, at room temperature, which exhibited a weak temperature dependence [8,9]. Such properties enable it to be a candidate thermoelectric material.

From a canonical point of view, lattice thermal conductivity is expected to decay in the region of high temperatures due to enhanced phonon-phonon scattering. In the case of GeSb$_2$Te$_4$, lattice thermal conductivity is observed to exhibit a weak variation as temperature increases from 300 to 773 K [8,9]. Therefore, it is desirable to elucidate how the lattice vibrations of GeSb$_2$Te$_4$ evolve as a function of temperature. Moreover, previous ARPES and theoretical studies have primarily focused on exploring the Dirac cone electronic structure [7,10]. However, due to the spontaneous formation of cation vacancies in this material, the Dirac point is far above the Fermi level in the real solid, leading to a shift of the Fermi level to the valence band [11–13]. As a result, electronic structures below the Fermi level have been the subject of limited experimental investigation. In particular, a detailed exploration of the band topology of the surface states below

the Fermi level remains necessary for a greater understanding of this material's potential applications.

In the present study, we synthesized high-quality single crystals of $GeSb_2Te_4$. The topological surface states were clearly identified below the Fermi level of $GeSb_2Te_4$ by means of ARPES and first-principles calculations. Such topological surface states were further observed to exhibit significant spin polarization by spin-resolved ARPES. Meanwhile, the weak temperature dependence of lattice thermal conductivity of $GeSb_2Te_4$ at high temperatures is primarily attributed to the weak thermal variation of the phonon lifetime of the low-energy phonons as revealed by both temperature-dependent Raman scattering measurement and lattice thermal conductivity calculations.

## II. EXPERIMENTAL AND COMPUTATIONAL DETAILS

High-quality single crystals of $GeSb_2Te_4$ were synthesized using the Bridgman method, as described in detail in a prior work [8]. Synchrotron-based ARPES experiments were carried out at BL-13U, National Synchrotron Radiation Laboratory with a VG-SCIENTA Omicron DA30L photoelectron analyzer. A flat, shiny surface was achieved through *in situ* cleavage under a base pressure greater than $7 \times 10^{-11}$ mbar. The overall energy resolution was greater than 20 meV and the angular resolution was $0.3\,°$. The chemical potential of our samples was referenced by gold on sample holders. Spin-resolved ARPES measurements were performed on a multichannel very-low-energy electron diffraction spin polarimeter using a helium discharge lamp as the light source [14]. Time-of-flight neutron powder diffraction experiments were performed on a BL-09 SPICA powder diffractometer in the Japan Proton Accelerator Research Complex (J-PARC). Rietveld refinements were performed using the Z-Rietveld software suite [15]. Temperature-dependent Raman spectra from 113 to 723 K were collected by a LabRAM Horiba HR Evolution spectrometer with an excitation wavelength of 532 nm. The laser power was maintained below 2 mW to avoid local heating of the sample. Before the measurement, the spectrometer was calibrated by measuring the 520.7 $cm^{-1}$ line of a silicon single crystal. During the measurement at more than room temperature, argon gas was loaded into the sample chamber to avoid oxidation of the specimen. The spectral resolution was greater than 1 $cm^{-1}$. Low-temperature (2 to 200 K) specific heat measurements were performed on a quantum design physical property measurement system using a standard thermal relaxation method.

The bulk electronic structures calculations were performed in the framework of density functional theory (DFT) using the projector augmented wave method [16] as implemented in the Vienna *ab initio* Simulation Package [17]. The generalized gradient approximation of Perdew-Burke-Ernzerhof [18] type was adopted for the exchange-correlation functional. The cutoff energy was set to 450 eV and the Brillouin zone integration was performed on a Monkhorst-Pack $k$-point mesh of $10 \times 10 \times 10$. Experimentally determined lattice parameters at $T = 20$ K were used with relaxed atomic positions. The spin-orbit coupling effect is included in our first-principles calculations. The tight binding model based on maximally localized Wannier functions [19,20] was constructed to

reproduce the spectral functions with the selection of germanium $s$ and $p$, antimony $p$, and tellurium $p$ orbitals. The surface states were calculated with surface Green function methods [21,22] as implemented in WANNIERTOOLS [23]. The parity analysis was performed using IRVSP code [24].

To obtain the lattice vibrational properties, the conventional unit cell was fully relaxed until the force was less than $2 \times 10^{-5}$ eV/Å. The DFT-D3 with the Becke-Johnson damping function was adopted for the van der Waals interaction [25]. The cutoff energy was set to 450 eV and the Brillouin zone integration was performed on a Monkhorst-Pack $k$-point mesh of $10 \times 10 \times 6$. The fully relaxed lattice parameters are $a = b = 4.249$ Å and $c = 40.163$ Å, which agrees well with our experimental data ($a = b = 4.218$ Å and $c = 40.875$ Å at $T = 20$ K). The phonon dispersion and heat capacity were then acquired with PHONOPY [26] using a $4 \times 4 \times 1$ supercell containing 336 atoms. To compute lattice thermal conductivity further, third-order interatomic force constants were extracted with a $4 \times 4 \times 1$ supercell, a $2 \times 2 \times 1$ $k$-point, and a 450-eV cutoff energy. According to a previous study on $Ge_2Sb_2Te_5$ by Mukhopadhyay *et al.* [27], we consider the interaction up to the fifth nearest neighboring atoms. Lattice thermal conductivity and phonon lifetime ware calculated by solving the phonon Boltzmann transport equation using the ShengBTE package [28].

## III. RESULTS AND DISCUSSIONS

$GeSb_2Te_4$ crystallizes in a layered rhombohedral crystal structure of space group $R\bar{3}m$ (No. 166), with seven alternating anion and cation layers stacking together along the $c$-axis. In early days, Agaev and Talybov proposed that the atoms stack in the sequence of Sb-Te-Te-Ge-Te-Te-Sb [see Fig. 1(a)] [29], then Kooi and De Hosson [30] suggested an alternative stacking of Te-Sb-Te-Ge-Te-Sb-Te [see Fig. 1(b)], which has been widely adopted. To determine the atomic distributions in our samples, we conducted neutron powder diffraction measurements on $GeSb_2Te_4$. Before conducting the experiments, the high quality of the sample was preliminarily examined by core-level spectroscopy measurements with sharp peaks of tellurium $4d$, antimony $4d$, and germanium $3d$ core levels [Fig. 1(c)]. Figures 1(e) and 1(g) display the Rietveld refinements of the neutron powder diffraction patterns collected at $T = 20$ K using the Agaev and Kooi models, respectively. Both the Agaev and Kooi models yield a good fit, with reliability factors $R_{wp} = 3.5\%$ and $3.34\%$, respectively. These results underscore the challenges of resolving the atomic sequence in $GeSb_2Te_4$ by means of neutron powder diffraction. Figures 1(f) and 1(h) show the calculated bulk electronic structures along high-symmetry directions using the Kooi and Agaev models, respectively. The high-symmetry points of the Brillouin zone are illustrated in Fig. 1(d). Interestingly, the aforementioned two kinds of atomic sequences present distinct electronic structures. As seen in Fig. 1(f), the calculated electronic structures of the Agaev sequence exhibit a metallic feature, while the bulk bands of the Kooi sequence shown in Fig. 1(h) host semiconducting characteristics with a narrow bandgap at the $Z$-point. Although high-resolution transmission microscopy can also reveal its atomic distribution [12], it turns out that electronic structures provide an alternative
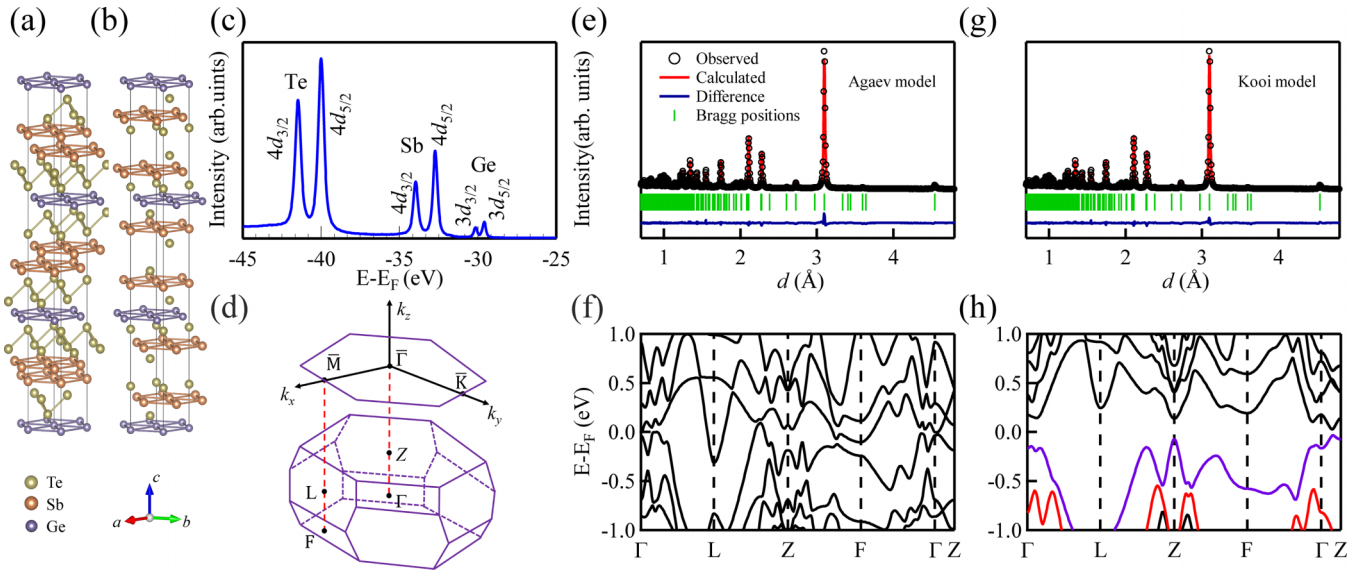
FIG. 1. (a) and (b) Crystal structure of the crystalline phase of GeSb$_2$Te$_4$ with the Agaev sequence and Kooi sequence, respectively. (c) Core-level photoemission spectrum of crystalline GeSb$_2$Te$_4$. (d) Bulk Brillouin zone of GeSb$_2$Te$_4$. (e) Rietveld refinements of the neutron diffraction data and (f) calculated bulk band structures along high-symmetry directions using the Agaev model. (g) and (h) Same as panels (e) and (f), but using the Kooi model. The neutron powder diffraction patterns shown in Fig. 1 are at $T = 20$ K.

way to identify the atomic distribution in the septuple layer of GeSb$_2$Te$_4$.

ARPES is a powerful technique for directly probing electronic band structures in crystalline solids. In this regard, we have performed systematic ARPES measurements on single crystalline GeSb$_2$Te$_4$. The Fermi surface mapping of GeSb$_2$Te$_4$ measured at an incident photon energy of 20 eV is depicted in Fig. 2(a). It is composed of a circular-like pocket centered at the $\bar{\Gamma}$-point and sixfold petal-like pockets along the $\bar{\Gamma}$-$\bar{M}$ direction. When moving toward the binding energy of 0.1 eV, the circular-like pocket evolves into a hexagon with a strong spectral weight [see Fig. 2(d)]. To compare the ARPES contours at constant energies with calculations, the calculated ones using the Kooi and Agaev models are depicted in Figs. 2(b), 2(c), 2(e), and 2(f). Here, it should be mentioned that the calculated Fermi level was shifted downward by 0.4 eV to have greater comparison with the experiments. The calculated contours show excellent agreement with the experimental data when the Kooi model is adopted. This unambiguously proves that the atomic distributions of crystalline GeSb$_2$Te$_4$ conform to the sequence proposed by Kooi.

Figure 2(g) illustrates the photoemission intensity plots taken along the $\bar{\Gamma}$-$\bar{M}$ direction. In fact, according to previous studies, a Dirac cone will appear at 0.45 eV above the Fermi level [7] [see our calculation in Fig. 2(h)]. Unfortunately, such a Dirac cone cannot be detected by our ARPES measurement, which is also not the scope of this work. Notably, double M-shaped bands with a strong spectral weight are evident, with the band top located at $\sim 0.1$ eV below the Fermi level. To determine the dimensionality of the M-shaped bands, we performed energy-dependent ARPES measurements along the $\bar{\Gamma}$-$\bar{M}$ direction. The M-shaped bands do not show evident variation as a function of incident photon energies, which supports their two-dimensional nature (see Supplemental Material Fig. S1 [31]). Furthermore, a comparison between the band

calculations of bulk (see Supplemental Material Fig. S2 [31]) and tellurium-terminated surface projection [see Figs. 2(h) and 2(i)] clearly shows that the M-shaped bands match well with the calculation of tellurium-terminated surface states, demonstrating the surface origin of those bands. Moreover, it is intriguing to know whether such M-shaped surface bands possess a topological nature. Given that the nonmagnetic property with time-reversal symmetry in GeSb$_2$Te$_4$, and the M-shaped surface bands lie between bulk band 38 [purple band in Fig. 1(h)] and band 36 [red band in Fig. 1(h)], we therefore employed the Fu-Kane method [32] to elucidate the nature of the topology for occupied bulk band 36. As illustrated in Table I, our parity analysis shows that band 36 hosts a topological nontrivial property with topological invariant $Z_2 = 1$, which indicates the topological nontrivial characteristic of the M-shaped surface states.

Topological surface states can exhibit helical spin textures. Figure 3(a) shows the spin-resolved ARPES spectra along the $\bar{\Gamma}$-$\bar{M}$ direction for the spin direction perpendicular to the momentum ($y$ spin polarization). It is evident that the upper M-shaped bands show the spin spectral weight with striking contrast on both sides. Such a characteristic can be better

TABLE I. Calculated parity at eight time-reversal invariant momenta points and the $Z_2$ invariant for occupied bands 36 and 38. Here, it should be noted that three $F$ and $\Gamma$ points are equivalent due to the crystalline symmetry of GeSb$_2$Te$_4$. we thus show the calculated parity values at the $\Gamma$, $F$, $L$, and $Z$ points.

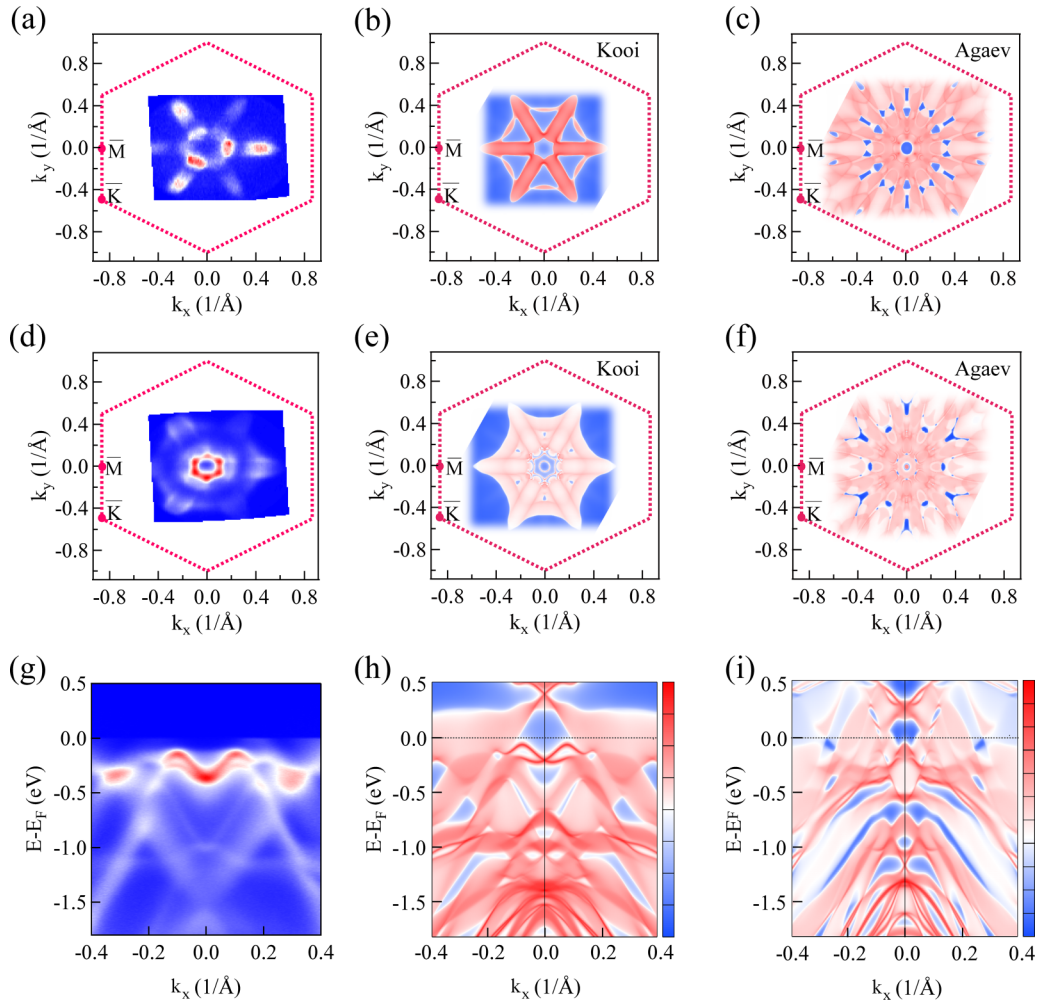| Occupied band | Parity (prod.) | | | | Invariant |
|---|---|---|---|---|---|
| | $\delta_\Gamma$ | $\delta_F$ | $\delta_L$ | $\delta_Z$ | $Z_2$ |
| 38 | − | − | − | + | 1 |
| 36 | + | − | − | − | 1 |

FIG. 2. (a) and (d) Experimental contour mapping of constant energies at the Fermi level and a binding energy of 0.1 eV, measured at $T = 25$ K with an incident photon energy of 20 eV. (b) and (e) Theoretical calculated contour mapping with constant energies at the Fermi level and a binding energy of 0.1 eV using the Kooi sequence. (c) and (f) Same as panels (b) and (e), but using the Agaev sequence. (g) Experimental ARPES intensity along the $\bar{M}$-$\bar{\Gamma}$-$\bar{M}$ direction. (h) Calculated bulk bands with tellurium termination surface states along the $\bar{M}$-$\bar{\Gamma}$-$\bar{M}$ direction using the Kooi sequence. (i) Calculated bulk bands with tellurium termination surface states along the $\bar{M}$-$\bar{\Gamma}$-$\bar{M}$ direction using the Agaev sequence.

visualized in the momentum distribution curves of the spin polarization at a binding energy of 0.2 eV, as shown in Fig. 3(b). The spin polarization reaches a maximum value of 60%. Figure 3(c) presents the calculated in-plane spin textures from the upper M-shaped bands, which is in good agreement with our experimental data, where the right and left sides of the momenta are dominated by the spin-up and spin-down intensities, respectively. In fact, the lower M-shaped topological surface bands are also expected to show the spin polarization characteristic. However, because the lower M-shaped bands are close to the bulk banks with weaker spectral intensity compared to the upper M-shaped bands, their spin polarization cannot be distinguished in our measurement. Considering that the distribution of germanium/antimony atoms in GeSb$_2$Te$_4$, our data suggest that the M-shaped topological surface states are robust against the intermixing effect of germanium/antimony atoms. In future studies, such topological surface states can be potentially utilized to develop spintronic devices by manipulating them to the Fermi level using voltage bias in thin films.

Next, we turn to the thermodynamic behavior of GeSb$_2$Te$_4$. Figure 4 presents the specific heat of GeSb$_2$Te$_4$ as a function of temperature. In a nonmagnetic system, the specific heat is primarily composed of contributions from electron, phonon, volume change (induced by thermal expansion), and phonon anharmonicity [33]. From the calculated phonon spectra (see Supplemental Material Fig. S3 [31]), we are able to obtain the lattice vibrational heat capacity. As illustrated in Fig. 4(a), the experimental specific heat is well reproduced by the lattice vibrational contribution [blue line in Fig. 4(a)], indicating that other factors make negligible contributions to the heat capacity in this temperature region. Figure 4(b) displays the $C_P/T$ versus $T^2$ plot from 2 to 5.8 K, and the data can be modeled using the Debye model $C_P/T = \alpha + \delta\ T^2 + \varepsilon T^4$ [34,35]. Here, the first term corresponds to the electronic contribution, with $\alpha$ being the Sommerfeld coefficient, and the second and third terms represent the lattice contributions. The fitting yields $\alpha = 0.78$ mJ mol$^{-1}$ K$^{-2}$, $\delta = 1.83$ mJ mol$^{-1}$ K$^{-4}$, and $\varepsilon = 3.0$ mJ mol$^{-1}$ K$^{-6}$. Since the
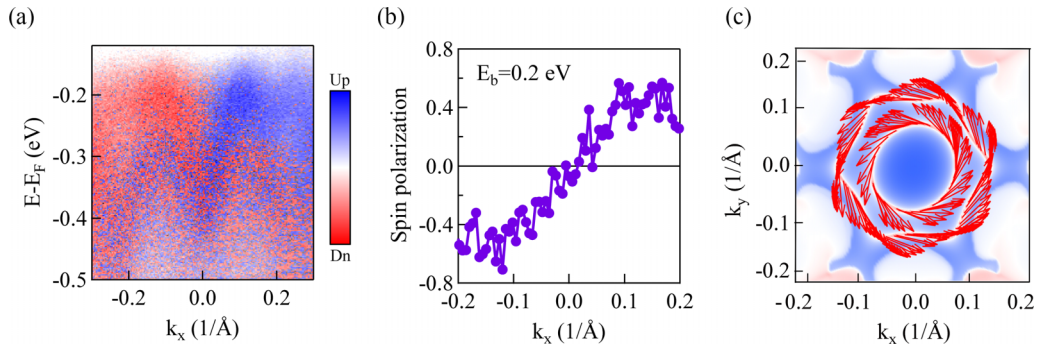
FIG. 3. (a) Spin-resolved ARPES intensity along the $\bar{M}$-$\bar{\Gamma}$-$\bar{M}$ direction measured at $T = 6$ K. The color scales represent the sign of the spin direction perpendicular to the momentum. (b) Momentum-dependent spin polarization at a binding energy of 0.2 eV. (c) Spin texture on a constant energy contour for the topological surface states at a binding energy of 0.08 eV. Red arrows denote spin orientations on $k_x$-$k_y$ plane.

Sommerfeld coefficient $\alpha$ reflects the magnitude of the effective mass of the carrier [36,37], the small value of $\alpha$ is a sign of the low effective mass of $GeSb_2Te_4$. This is in line with our observation that the linear-like bulk bands cross the Fermi level (see Supplemental Material Fig. S2(d) [31]).

The Debye temperature, $\theta_D = 195$ K, can be derived using the relation $\theta_D = \left(\frac{12\pi^4 Rn}{5\delta}\right)^{\frac{1}{3}}$, where $R$ is the gas constant and $n$ is the number of the atoms per formula unit. According to the Boltzmann transport theory, thermal conductivity is a product of phonon lifetime, heat capacity, and the square of phonon velocity, in which a low phonon velocity is favorable for achieving low lattice thermal conductivity. We can thus estimate the magnitude of the phonon velocity through the relation $v_s = \theta_D(\frac{k_B}{h})(\frac{4\pi}{3N}\frac{V}{})^{\frac{1}{3}}$ [38], where $h$, $k_B$, $N$, and $V$ correspond to Planck's constant, the Boltzmann constant, the number of the atoms per unit cell, and the volume of the unit cell, respectively. The phonon velocity is estimated to 1979 m/s, which is comparable to state-of-art thermoelectric materials such as PbTe and PbSe, for which the phonon velocity is 1794 and 1951 m/s, respectively [39]. Consequently, the low lattice thermal conductivity in $GeSb_2Te_4$ can be partially ascribed to its low phonon velocity. As we show later, the low lattice thermal conductivity is also correlated to its low phonon lifetime.

To get more insights about the thermal dependence of the lattice dynamics, we performed Raman scattering measurements on $GeSb_2Te_4$. Since the primitive cell contains seven atoms, the factor group analysis predicts 18 optical modes at the center of the Brillouin zone $\Gamma = 3E_g + 3E_u + 3A_{2u} + 3A_{1g}$. Among them, three doubly degenerate $E_g$ modes and three $A_{1g}$ modes belong to Raman-active modes. As illustrated in Fig. 5(a), five Raman-active vibrational modes are visible at $T = 113$ K, located at 35.23, 55.98, 109.28, 119.93, and 176.25 cm$^{-1}$. According to our calculations, the modes at 35.23 cm$^{-1}$, 55.98 cm$^{-1}$, 109.28 cm$^{-1}$, and 176.25 cm$^{-1}$ are assigned to the $E_g^1$, $A_{1g}^1$, $E_g^2$, and $A_{1g}^3$ modes, respectively (see Supplemental Material Fig. S4 for the atomic displacements of these Raman-active modes [31]). Regarding the mode at 119.93 cm$^{-1}$, it is challenging to determine its vibrational behavior because the calculated frequency of the $A_{1g}^2$ mode is almost identical to that of the $E_g^3$ mode (see Supplemental Material Table SI [31]). Additionally, as the temperature increases, the third and fourth Raman peaks merge together to form a single broad peak [see Raman spectra at $T = 303$ K in Fig. 5(a)], and we thus focus on the analysis of $E_g^1$, $A_{1g}^1$, and $A_{1g}^3$ modes.

Figure 5(b) displays the Raman spectra under various temperatures. It is apparent that the optical modes decrease in frequency with increasing temperature [see Figs. 5(d)–5(f)]. In general, the phonon softening behavior can be interpreted in terms of the implicit anharmonicity effect triggered by lattice thermal expansion, and the explicit anharmonicity (or phonon anharmonicity) arising from the higher order terms in the interatomic potential [40,41]. The Balkanski model [42] has been widely used to study phonon anharmonicity in solids [43–47]. Accordingly, we adopted the Balkanski model to understand the temperature dependence of the phonon frequency,

$$\omega(T) = \omega_0 + \omega_0\left(\exp\left(-\gamma\int_0^T \beta(T)dT\right) - 1\right)$$
$$+ C\left[1 + \frac{2}{e^x - 1}\right] + D\left[1 + \frac{3}{e^y - 1} + \frac{3}{(e^y - 1)^2}\right],$$
(1)

where $x = \frac{\hbar\omega_0}{2k_BT}$, $y = \frac{\hbar\omega_0}{3k_BT}$, and $\omega_0$ is the frequency of an optical mode at $T = 0$ K. The second term stands for the
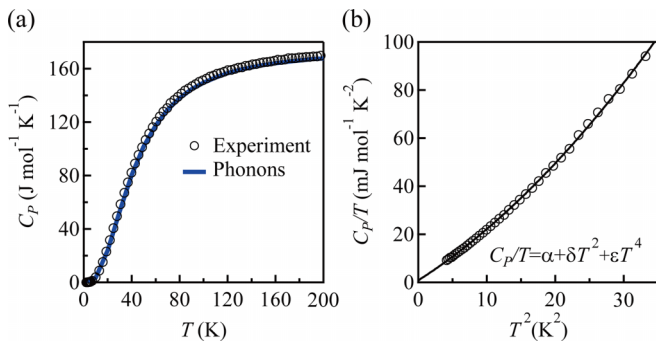


FIG. 4. (a) Temperature dependence of the heat capacity. The blue line represents the calculated heat capacity at constant volume arising from the lattice vibrations. (b) $C_P/T$ versus $T^2$ plot in the low-temperature region from 2 to 5.8 K. The black line is a fit using $C_P/T = \alpha + \delta T^2 + \varepsilon T^4$.
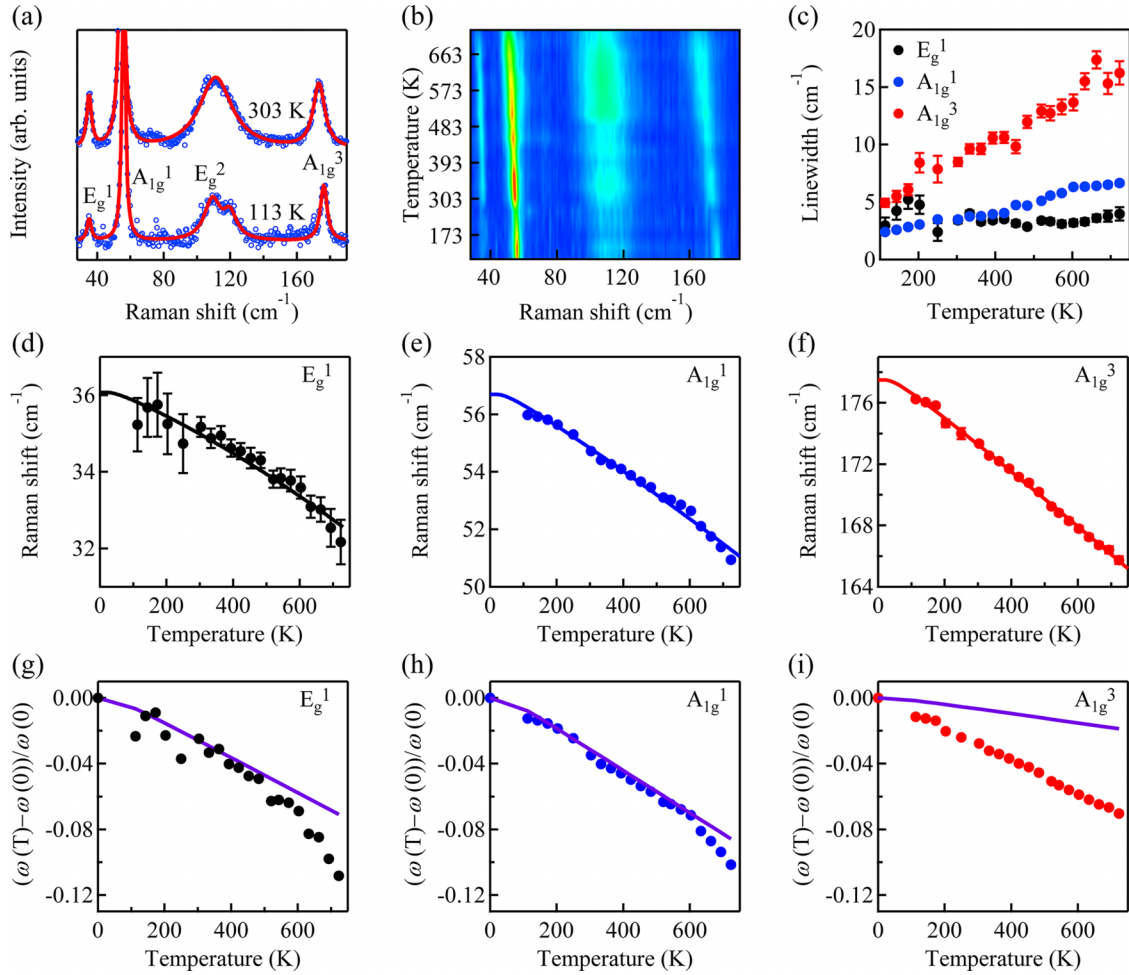
FIG. 5. (a) Raman spectra of GeSb$_2$Te$_4$ measured at $T = 113$ and 303 K. The blue empty symbols represent the experimental data and the red line is the fit with multiple Lorentzian functions. (b) Temperature-dependent Raman intensity plot. (c) The temperature dependence of the linewidths of the E$_g^1$, A$_{1g}^1$, and A$_{1g}^3$ modes. (d)–(f) The thermal evolution of the peak frequencies of the E$_g^1$, A$_{1g}^1$ and A$_{1g}^3$ modes. The solid line is the fit of the temperature-dependent peak frequencies using Eq. (1). (g)–(i) Normalized temperature dependence of the peak frequencies of the E$_g^1$, A$_{1g}^1$ and A$_{1g}^3$ modes. The peak frequencies at $T = 0$ K are extracted by extrapolating the fit to 0 K using Eq. (1). The thermal expansion contribution to the phonon softening is plotted as the purple line.

volume thermal expansion contribution, and the third and fourth terms are phonon anharmonicity contributions. Here, $\beta$ is the thermal expansion coefficient, which can be derived from the refinements of our temperature-dependent neutron powder diffraction data (see Supplemental Material Fig. S5 [31]), and $\gamma$ is the mode Grüneisen parameters. To the best of our knowledge, the experimental mode Grüneisen parameters of GeSb$_2$Te$_4$ have not been reported so far. Due to the fact that the lattice dynamic behavior of GeSb$_2$Te$_4$ resembles that of SnSb$_2$Te$_4$, including the frequencies of the vibrational modes, we referred to the studies by Sans *et al.* [48], in which the mode Grüneisen parameters are 2.05, 2.5, and 0.53 for the E$_g^1$, A$_{1g}^1$ and A$_{1g}^3$ modes, respectively.

As shown in Figs. 5(d)–5(f), the phonon softening behaviors are well fitted by the Balkanski model. The thermal expansion contributions to the phonon softening of each mode are plotted in Figs. 5(g)–5(i). It is clear that the thermal expansion (the purple line) plays a dominate role in the softening of the E$_g^1$ and A$_{1g}^1$ modes. In contrast, the phonon

anharmonicity contributes more to the phonon softening of the A$_{1g}^3$ mode. The phonon linewidth illustrates the broadening of the spectral peak of a specific phonon mode, which is caused by the interaction of the phonon with other phonons, in addition to defects and impurities. The change in phonon linewidth with temperature is determined by anharmonic phonon-phonon scattering [43–47], which facilitates the analysis of the phonon softening based on the Balkanski model. As seen in Fig. 5(c), the linewidths of the E$_g^1$ and A$_{1g}^1$ modes exhibit only slight variation over a wide temperature range from 113 to 723 K. Nevertheless, the linewidth of the A$_{1g}^3$ mode exhibits a strong temperature dependence. Our data suggest that the low-lying phonon modes do not exhibit evident enhancement in phonon-phonon scattering with temperature. Such an observation is in line with the analysis of phonon softening.

To gain a better understanding of the role of the low-lying optical phonons in the heat conduction of GeSb$_2$Te$_4$, we calculated the lattice thermal conductivity by solving the
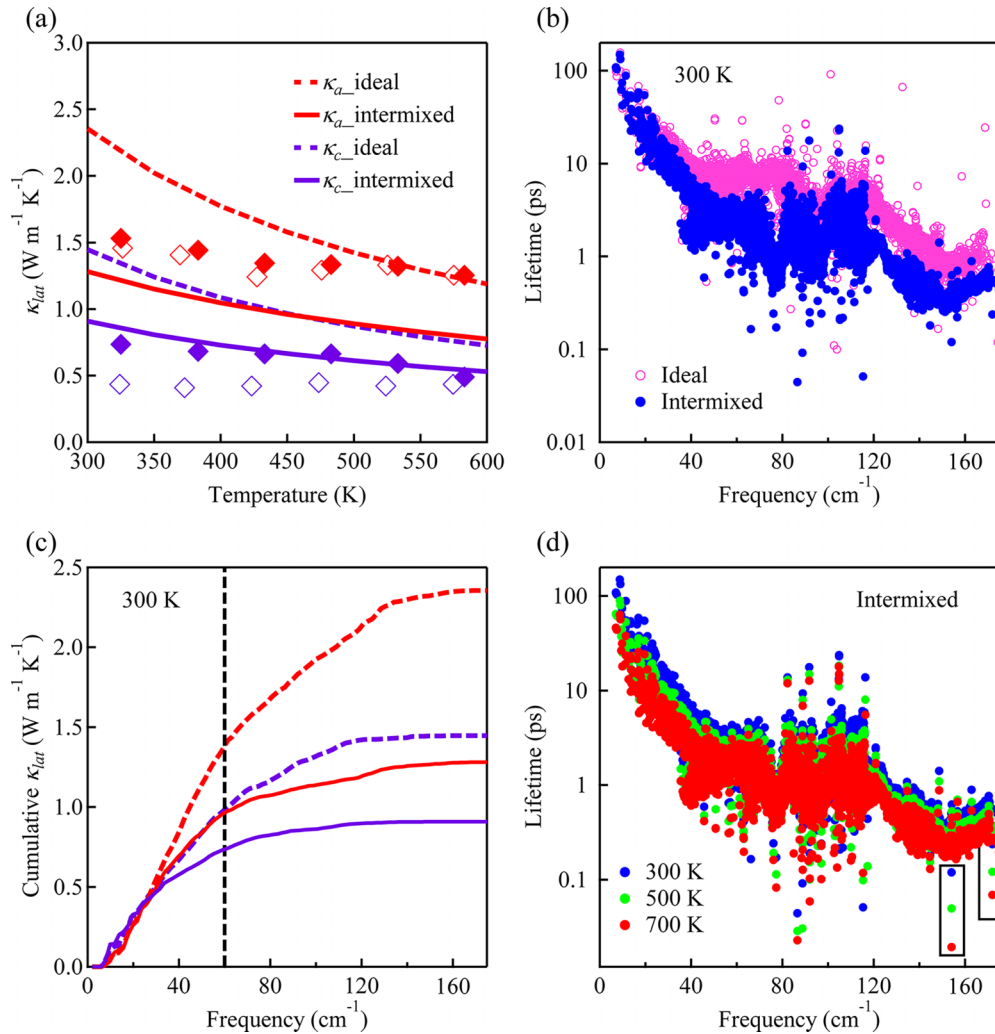
FIG. 6. (a) Calculated lattice thermal conductivity of $GeSb_2Te_4$ along the $a$- and $c$-axes as a function of temperature. The symbols are experimental data extracted from Refs. [8] and [9]. The dashed lines are the calculated lattice thermal conductivity using the ideal Kooi sequence; the solid lines are the calculated lattice thermal conductivity when the intermixing effect is considered. (b) Frequency dependence of phonon lifetime at $T = 300$ K. The pink empty symbols represent the calculated phonon lifetime using the ideal Kooi sequence; the blue solid symbols represent the calculated phonon lifetime when the intermixing effect is considered. (c) Cumulative lattice thermal conductivity versus frequency along the $a$- and $c$-axes at $T = 300$ K. (d) Frequency dependence of the phonon lifetime at $T = 300$, $500$, and $700$ K when the intermixing effect is considered.

phonon Boltzmann transport equation. Although the intermixing effect has a weak impact on the electronic structures (see Supplemental Material Fig. S6 [31]), it affects thermal transport by scattering the phonons. As a result, we initially calculated the lattice thermal conductivity using the ideal Kooi model. As depicted in Fig. 6(a), the calculated lattice thermal conductivity decays obviously as a function of temperature, and those values are found to be larger than the experimental data. To address the impact of the intermixing effect of geranium/antimony atoms, we referred to a prior theoretical work on $Ge_2Sb_2Te_5$ by Campi *et al.* [49] and treated it as isotopic impurities scattering. Consequently, the lattice thermal conductivity at $T = 300$ K decreased from 2.35 to 1.28 W m$^{-1}$ K$^{-1}$ for the $a$-axis and from 1.45 to 0.91 W m$^{-1}$ K$^{-1}$ for the $c$-axis, which are in good agreement with the experimental data. As illustrated in Fig. 6(b), the decline in lattice thermal conductivity arises from the reduction in phonon lifetime above 30 cm$^{-1}$. Figure 6(c) presents the

cumulative lattice thermal conductivity versus the frequency along the $a$- and $c$-axes for both the ideal Kooi and intermixed cases. The modes below 60 cm$^{-1}$ contribute 75% and 81% to the lattice thermal conductivity along the $a$- and $c$-axes, respectively, when the intermixing effect is considered, revealing that heat conduction is dominated by the low-lying phonon modes. In addition, as depicted in Fig. 6(d), we also extracted the phonon lifetime at several temperatures. While the phonon lifetime decreases evidently for some high-energy phonons [indicated by black rectangles in Fig. 6(d)], the lifetime of most phonons does not show significant changes when the temperature changes from 300 to 700 K, which is due to phonon-germanium/antimony disorder scattering. Such observation is in line with our Raman data. We thus argue that the weak temperature dependence of the lattice thermal conductivity of $GeSb_2Te_4$ at high temperatures is correlated to the weak thermal variation of the linewidth of the low-energy phonons.

## IV. CONCLUSION

In this work, we carried out a systematic investigation of the electronic structures and lattice vibrational behaviors of crystalline $GeSb_2Te_4$ using ARPES, heat capacity, and Raman scattering measurements, as well as first-principles calculations. Notably, our observations revealed M-shaped topological surface states with significant spin polarization located near the Fermi level, presenting a potential avenue for spintronic devices. Through an analysis of the heat capacity data, we found that the low lattice thermal conductivity can be partially attributed to the low phonon velocity. Furthermore, the analysis of the temperature-dependent Raman-active modes suggests that the thermal expansion effect is the primary driving factor behind the softening of the low-energy $A_{1g}^1$ and $E_g^1$ phonon modes. Meanwhile, their phonon linewidth does not exhibit notable changes with increasing temperatures, indicating the weak temperature-dependent phonon anharmonicity of these modes. Our lattice thermal conductivity calculation further supports this finding, as it reveals that the modes below 60 cm$^{-1}$ contribute mostly to thermal transport, and the phonon lifetime does not show apparent variation with temperature. Based on these results, we believe that minor variation in lattice thermal conductivity at high temperatures can be primarily attributed to weak temperature-dependent phonon anharmonicity. Our study provides new insights into the electronic structures and lattice dynamics of $GeSb_2Te_4$, which could be crucial for its potential technological applications.

[1] M. Wuttig and N. Yamada, Phase-change materials for rewriteable data storage, Nat. Mater. **6**, 824 (2007).

[2] D. Lencer, M. Salinga, B. Grabowski, T. Hickel, J. Neugebauer, and M. Wuttig, A map for phase-change materials, Nat. Mater. **7**, 972 (2008).

[3] S. Raoux, W. Welnic, and D. Ielmini, Phase change materials and their application to nonvolatile memories, Chem. Rev. **110**, 240 (2010).

[4] T. Siegrist, P. Jost, H. Volker, M. Woda, P. Merkelbach, C. Schlockermann, and M. Wuttig, Disorder-induced localization in crystalline phase-change materials, Nat. Mater. **10**, 202 (2011).

[5] J. Kim and S.-H. Jhi, Emerging topological insulating phase in Ge-Sb-Te compounds, Phys. Status Solidi B **249**, 1874 (2012).

[6] S. V. Eremeev *et al.*, Atom-specific spin mapping and buried topological states in a homologous series of topological insulators, Nat. Commun. **3**, 635 (2012).

[7] M. Nurmamat *et al.*, Topological nontrivial phase-change compound $GeSb_2Te_4$, ACS Nano **14**, 9059 (2020).

[8] Y. Chen, B. Zhang, Y. Zhang, H. Wu, K. Peng, H. Yang, Q. Zhang, X. Liu, Y. Chai, X. Lu, G. Wang, Z. Zhang, J. He, X. Han, and X. Zhou, Atomic-scale visualization and quantification of configurational entropy in relation to thermal conductivity: A proof-of-principle study in t-$GeSb_2Te_4$, Adv. Sci. **8**, 2002051 (2021).

[9] P. Chen, H. Wu, B. Zhang, Z. Zhou, S. Zheng, L. Dai, Y. Huo, D. Zhang, Y. Yan, K. Peng, G. Han, X. Lu, X. Zhou, and G. Wang, Intrinsically low lattice thermal conductivity and anisotropic thermoelectric performance in In-doped $GeSb_2Te_4$ single crystals, Adv. Funct. Mater. **33**, 2211281 (2023).

[10] L.-L. Wang, Highly tunable band inversion in $AB_2X_4$ ($A$ = Ge, Sn, Pb; $B$ = As, Sb, Bi; $X$ = Se, Te) compounds, Phys. Rev. Mater. **6**, 094201 (2022).

[11] Z. Sun, Y. Pan, J. Zhou, B. Sa, and R. Ahuja, Origin of *p*-type conductivity in layered *n*GeTe-*m*$Sb_2Te_3$ chalcogenide semiconductors, Phys. Rev. B **83**, 113201 (2011).

[12] J.-J. Wang, J. Wang, H. Du, L. Lu, P. C. Schmitz, J. Reindl, A. M. Mio, C.-L. Jia, E. Ma, R. Mazzarello, M. Wuttig, and W. Zhang, Genesis and effects of swapping bilayers in hexagonal $GeSb_2Te_4$, Chem. Mater. **30**, 4770 (2018).

[13] T.-R. Wei, P. Hu, H. Chen, K. Zhao, P. Qiu, X. Shi, and L. Chen, Quasi-two-dimensional GeSbTe compounds as promising thermoelectric materials with anisotropic transport properties, Appl. Phys. Lett. **114**, 053903 (2019).

[14] H. Zha, W. Liu, D. Wang, B. Zhao, X. Shen, M. Ye, and S. Qiao, Improvement of image-type very-low-energy-electron-diffraction spin polarimeter, Rev. Sci. Instrum. **94**, 073704 (2023).

[15] R. Oishi, M. Yonemura, Y. Nishimaki, S. Torii, A. Hoshikawa, T. Ishigaki, T. Morishima, K. Mori, and T. Kamiyama, Rietveld analysis of software for J-PARC, Nucl. Instrum. Methods. Phys. Res. Sect. A. **600**, 94 (2009).

[16] P. Blöchl, Projector augmented-wave method, Phys. Rev. B **50**, 17953 (1994).

[17] G. Kresse and J. Furthmüller, Efficient iterative schemes for *ab initio* total-energy calculations using a plane-wave basis set, Phys. Rev. B **54**, 11169 (1996).

[18] J. P. Perdew, K. Burke, and M. Ernzerhof, Generalized Gradient Approximation Made Simple, Phys. Rev. Lett. **77**, 3865 (1996).

[19] N. Marzari and D. Vanderbilt, Maximally localized generalized Wannier functions for composite energy bands, Phys. Rev. B **56**, 12847 (1997).

[20] I. Souza, N. Marzari, and D. Vanderbilt, Maximally localized Wannier functions for entangled energy bands, Phys. Rev. B **65**, 035109 (2001).

[21] M. P. L. Sancho, J. M. L. Sancho, and J. Rubio, Quick iterative scheme for the calculation of transfer matrices:

Application to Mo (100), J. Phys. F Met. Phys. **14**, 1205 (1984).

[22] M. P. L. Sancho, J. M. L. Sancho, and J. Rubio, Highly convergent schemes for the calculation of bulk and surface Green-functions, J. Phys. F: Met. Phys. **15**, 851 (1985).

[23] Q. Wu, S. Zhang, H.-F. Song, M. Troyer, and A. A. Soluyanov, WannierTools: An open-source software package for novel topological materials, Comput. Phys. Commun. **224**, 405 (2018).

[24] J. Gao, Q. Wu, C. Persson, and Z. Wang, Irvsp: To obtain irreducible representations of electronic states in the VASP, Comput. Phys. Commun. **261**, 107760 (2021).

[25] S. Grimme, S. Ehrlich, and L. Goerigk, Effect of the damping function in dispersion corrected density functional theory, J. Comput. Chem. **32**, 1456 (2011).

[26] A. Togo and I. Tanaka, First principles phonon calculations in materials science, Scripta Mater. **108**, 1 (2015).

[27] S. Mukhopadhyay, L. Lindsay, and D. J. Singh, Optic phonons and anisotropic thermal conductivity in hexagonal $Ge_2Sb_2Te_5$, Sci. Rep. **6**, 37076 (2016).

[28] W. Li, J. Carrete, N. A. Katcho, and N. Mingo, ShengBTE: A solver of the Boltzmann transport equation for phonons, Comput. Phys. Commun. **185**, 1747 (2014).

[29] K. A. Agaev and A. G. Talybov, Electron-diffraction analysis of structure of $GeSb_2Te_4$, Sov. Phys. Crystallogr. **11**, 400 (1966).

[30] B. J. Kooi and J. Th. M. De Hosson, Electron diffraction and high-resolution transmission electron microscopy of the high temperature crystal structures of $Ge_xSb_2Te_{3+x}$ ($x = 1, 2, 3$) phase change materials, J. Appl. Phys. **92**, 3584 (2002).

[31] See Supplemental Material at http://link.aps.org/supplemental/10.1103/PhysRevB.108.054311 for the ARPES intensity along the $M$-$\Gamma$-$M$ direction taken with various photon energies, the calculated bulk projected and surface states with the tellurium termination along the $M$-$\Gamma$-$M$ direction, the calculated phonon dispersion along high-symmetry directions using the Kooi sequence, atomic displacements of these Raman-active modes, temperature dependence of lattice parameters and the thermal expansion coefficient, the calculated bulk band structures along high-symmetry directions using the Kooi and intermixed models, and a comparison of the optical phonon frequencies between the experiments and calculation.

[32] L. Fu and C. L. Kane, Topological insulators with inversion symmetry, Phys. Rev. B **76**, 045302 (2007).

[33] P. Jund, R. Viennois, X. Tao, K. Niedziolka, and J.-C. Tédenac, Physical properties of thermoelectric zinc antimonide using first-principles calculations, Phys. Rev. B **85**, 224105 (2012).

[34] A. Pandey, D. G. Quirinale, W. Jayasekara, A. Sapkota, M. G. Kim, R. S. Dhaka, Y. Lee, T. W. Heitmann, P. W. Stephens, V. Ogloblichev, A. Kreyssig, R. J. McQueeney, A. I. Goldman, A. Kaminski, B. N. Harmon, Y. Furukawa, and D. C. Johnston, Crystallographic, electronic, thermal, and magnetic properties of single-crystal $SrCo_2As_2$, Phys. Rev. B **88**, 014526 (2013).

[35] S. Misra, B. Wiendlocha, J. Tobola, P. Levinský, J. Hejtmánek, S. Migot, J. Ghanbaja, A. Dauscher, B. Lenoir, and C. Candolfi, Influence of In-induced resonant level on the normal-state

and superconducting properties of $Sn_{1.03}Te$, Phys. Rev. B **106**, 075205 (2022).

[36] M. Ahrens, R. Merkle, B. Rahmati, and J. Maier, Effective masses of electrons in $n$-type $SrTiO_3$ determined from low-temperature specific heat capacities, Physica B **393**, 239 (2007).

[37] W. Liu, X. Tan, K. Yin, H. Liu, X. Tang, J. Shi, Q. Zhang, and C. Uher, Convergence of Conduction Bands as a Means of Enhancing Thermoelectric Performance of $n$-type $Mg_2Si_{1-x}Sn_x$ Solid Solutions, Phys. Rev. Lett. **108**, 166601 (2012).

[38] K. Kurosaki, A. Kosuga, H. Muta, M. Uno, and S. Yamanaka, $Ag_9TlTe_5$: A high-performance thermoelectric bulk material with extremely low thermal conductivity, Appl. Phys. Lett. **87**, 061919 (2005).

[39] Y. Xiao, C. Chang, Y. Pei, D. Wu, K. Peng, X. Zhou, S. Gong, J. He, Y. Zhang, Z. Zeng, and L.-D. Zhao, Origin of low thermal conductivity in SnSe, Phys. Rev. B **94**, 125203 (2016).

[40] A. Sanson, M. Giarola, G. Mariotto, L. Hu, J. Chen, and X. Xing, Lattice dynamics and anharmonicity of $CaZrF_6$ from Raman spectroscopy and *ab initio* calculations, Mater. Chem. Phys. **180**, 213 (2016).

[41] S. Kesari, N. P. Salke, S. J. Patwe, S. N. Achary, A. K. Sinha, P. U. Sastry, A. K. Tyagi, and R. Rao, Structural stability and anharmonicity of $Pr_2Ti_2O_7$: Raman spectroscopic and XRD studies, Inorg. Chem. **55**, 11791 (2016).

[42] M. Balkanski, R. F. Wallis, and E. Haro, Anharmonic effects in light scattering due to optical phonons in silicon, Phys. Rev. B **28**, 1928 (1983).

[43] F. Liu, P. Parajuli, R. Rao, P. C. Wei, A. Karunarathne, S. Bhattacharya, R. Podila, J. He, B. Maruyama, G. Priyadarshan, J. R. Gladden, Y. Y. Chen, and A. M. Rao, Phonon anharmonicity in single-crystalline SnSe, Phys. Rev. B **98**, 224309 (2018).

[44] M. A. Prosnikov, A. N. Smirnov, V. Yu. Davydov, and R. V. Pisarev, Magnetic dynamics and spin-phonon coupling in the antiferromagnet $Ni_2NbBO_6$, Phys. Rev. B **98**, 104404 (2018).

[45] Yu. S. Ponosov and D. Y. Novoselov, Lattice and spin excitations of $YFeO_3$: A Raman and density functional theory study, Phys. Rev. B **102**, 054418 (2020).

[46] H. Yu, L.-C. Chen, H.-J. Pang, P.-F. Qiu, Q. Peng, and X.-J. Chen, Temperature-dependent phonon anharmonicity and thermal transport in $CuInTe_2$, Phys. Rev. B **105**, 245204 (2022).

[47] M. Tiadi, D. P. Satapathy, and M. Battabyal, Evolution of optical phonon modes and thermoelectric properties in doped $Bi_2Te_3$: A temperature-dependent Raman spectroscopy study, Phys. Rev. Mater. **7**, 015401 (2023).

[48] J. A. Sans, R. Vilaplana, E. L. da Silva, C. Popescu, V. P. Cuenca-Gotor, A. Andrada-Chacón, J. Sánchez-Benitez, O. Gomis, A. L. J. Pereira, P. Rodríguez-Hernández, A. Muñoz, D. Daisenberger, B. García-Domene, A. Segura, D. Errandonea, R. S. Kumar, O. Oeckler, P. Urban, J. Contreras-García, and F. J. Manjón, Characterization and decomposition of the natural van der Waals $SnSb_2Te_4$ under compression, Inorg. Chem. **59**, 9900 (2020).

[49] D. Campi, L. Paulatto, G. Fugallo, F. Mauri, and M. Bernasconi, First-principles calculation of lattice thermal conductivity in crystalline phase change materials: GeTe, $Sb_2Te_3$, and $Ge_2Sb_2Te_5$, Phys. Rev. B **95**, 024311 (2017).